Contents lists available at ScienceDirect

Precambrian Research

journal homepage: www.elsevier.com/locate/precamres

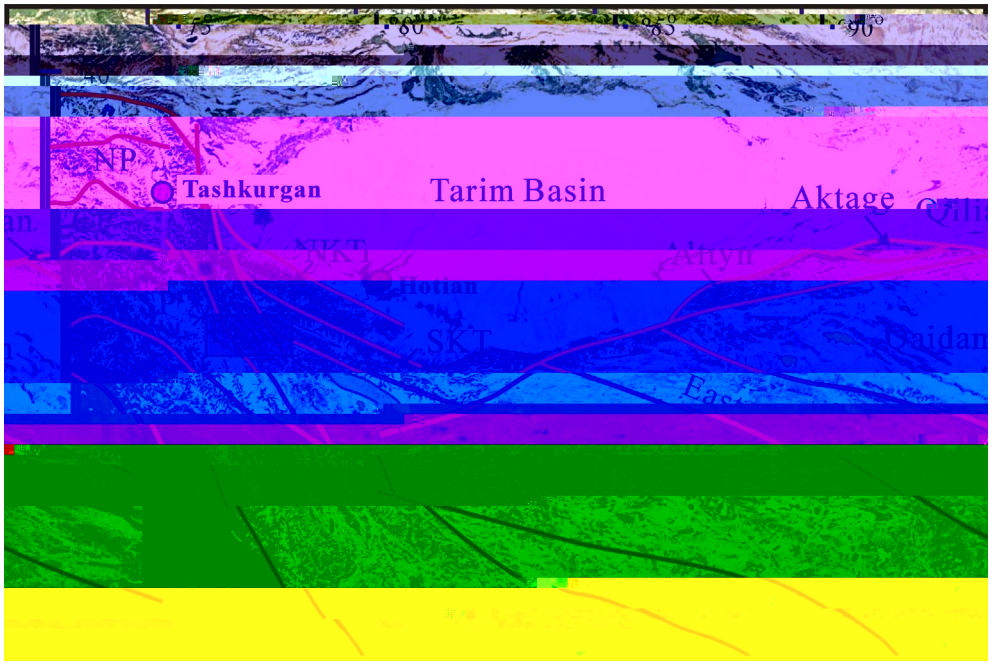

Fig. 1. Simplified tectonic map of the Tibetan Plateau showing the major terranes occupying Precambrian basement (modified after Robinson et al., 2012). NP-Northern Pamir, CP-Central Pamir, SP-Southern Pamir, NKT-Northern Kunlun terrane, SKT-Southern Kunlun terrane, TSHT-Tianshuihai terrane, LST-Lhasa terrane. The grey area marked in TSHT represents the Neoproterozoic Tianshuihai Group.

assemblages and tectonothermal history. Thus, the detailed structure, phases of igneous activity and metamorphism of the individual terrane could shed lights on understanding the evolution of the Tethys Ocean and the evolution of global Precambrian supercontinent.

As an important part of the Tibetan Plateau, the Pamir Syntax at the northwestern end of the India–Asia collision zone underwent long-time drifting, accretion and collision since early Paleozoic (or Sinian) and the final suturing and basin closure occurred during the Mesozoic (e.g. Schwab et al., 2004; Xiao et al., 2002, 2005; Zanchi and Gaetani, 2011; Robinson et al., 2016; Robinson 2015; Angiolini et al., 2013, 2015; Rutte et al., 2017; Li et al., 2017). The most important tectonic unit in Pamir Syntax is the Tashkuergan terrane (also termed as Tashkuergan-Tianshuihai terrane), in which the amphibolite-granulite facies metamorphic rocks were identified as the Precambrian basement (Xinjiang, 1993; Yang et al., 2010). However, recent works demonstrated that the basement of the Tashkuergan terrane was early Paleozoic volcanic-sedimentary sequence, which is an accretionary wedge formed during the southward subduction of the Proto-Tethys ocean (Zhang et al., 2017a). Although some metamorphic rocks were identified as Precambrian basement of the Pamir Syntax in Pakistan and Kyrgyzstan (e.g., Robinson et al., 2012), reliable geochronological data are still scare. In this contribution, we identify an early Precambrian terrane based on reliable geochronological and geochemical data from the southeastern margin of the Pamir Syntax. We document the detailed rock associations of this terrane and report systematic zircon U-Pb ages and Hf isotope compositions and whole-rock geochemistry of the Precambrian igneous rocks in this terrane. Based on these data, we reevaluate the main Precambrian tectonothermal events of this terrane and their relationship to the Precambrian supercontinent evolutions. More importantly, our study sheds new lights on the Precambrian geology in NW China and the evolution process of the Tethys Ocean.

2. Regional Geological background

The arcuate convex north salient of the Pamir, also known as NW section of the Western Kunlun Orogenic Belt (WKOB), has generally been divided into three tectonic units, *i.e.,* Northern, Central, and Southern Pamir (Fig. 1) (Burtman and Molnar, 1993; Schwab et al., 2004; Robinson et al., 2007, 2016; Angiolini et al., 2015). The Northern Pamir was interpreted as a composite Paleozoic arc terrane equivalent to the Southern Kunlun terrane (Tapponnier et al., 1981; Boulin, 1988; Burtman and Molnar, 1993; Yin and Harrison, 2000). The possible correlation of the Central Pamir terrane to other tectonic units in eastern part of the WKOB remains unsolved. Central Pamir was regarded as (1) a separate terrane with no direct correlative body in Tibet (e.g., Burtman and Molnar, 1993), (2) the equivalent to the Songpan-Ganzi terrane (Yin and Harrison, 2000; Robinson et al., 2012), or (3) the equivalent to the Qiangtang terrane in Tibet (Schwab et al., 2004; Valli et al., 2008). The Southern Pamir-Karakoram terrane is generally interpreted to be continuous, although they may be separated by a suture zone or a region of highly attenuated continental crust from the Paleozoic rifting (Fig. 1, Zanchi et al., 2000).

In fact, the Central Pamir is dominated by the Muztaghata gneiss dome, locally termed as the Bulunkuole Group, which is regarded as a Precambrian basement and is equivalent to the Saitula Group, the Precambrian basement of the Southern Kunlun terrane (SKT) in eastern section of the WKOB, or equivalent to the Tianshuihai Group of the Tianshuihai terrane (Fig. 1) (Xinjiang, 1993; Qu et al., 2007; Ji et al., 2011). Systematic geochronological data have revealed that both the Bulunkuole Group and the Saitula Group were early Paleozoic accretionary wedges formed during the southward subduction of the Proto-Tethys oceanic crust (Zhang et al., 2017a, 2017b).

To south of the Muztaghata dome, Ji et al. (2011) identified a metamorphic bimodal volcanic sequence at Mazar. Zircons from the *meta*-rhyolite yield a Paleoproterozoic age of 2481 ± 14 Ma and a metamorphic age of 2016 ± 39 Ma. According to field observations, the early Precambrian sequence in Mazar was bounded by Neoproterozoic-Silurian faults on the south and was unconformably overlain by Permian rocks on the northeast. It was intruded by Mesozoic granites to the southeast and was sharply truncated by the north-south striking Tashkurgan fault on the northwest. The total outcropping area is less than 300 square kilometers and here we name it as Mazar terrane (Fig. 2). The northeastern part of the Mazar terrane mainly comprises of gneiss/schist with minor metamorphic bimodal volcanic rocks. In the southwest section, metamorphic bimodal volcanic rocks account for about ~ 80% of the total thickness (Ji et al., 2011). Main rock types include amphibolite (metabasalt), leptite (*meta*-rhyolite), biotite schist and biotite-plagioclase gneiss (Fig. 3a and b). Within most outcrops the bedding plane is well preserved in spite of amphibolite facies metamorphism (Fig. 3a). The Precambrian sequence was intruded by diverse

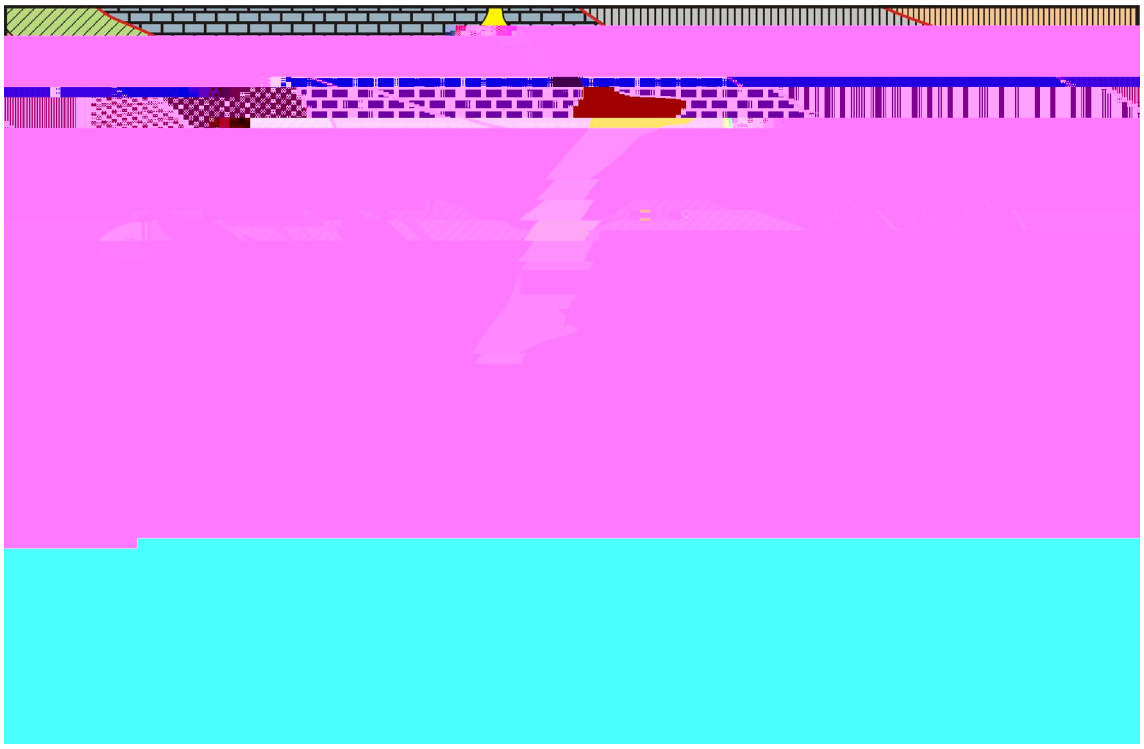

Fig. 2. Geological map of the Mazar terrane showing the Archaean basement and the Neoproterozoic granitic intrusions (geochronological sample locations are marked).

types of intrusions, including gabbros, diabase, tonalite and granodiorite (Fig. 3c and d). At one outcrop, we noticed a pegmatite intruding into the gneissic mafic intrusions (Fig. 3e). Bian et al. (2013) reported two zircon U-Pb ages of the granodiorites at 855 ± 14 Ma and 836 ± 12 Ma. As for the mafic intrusions, no ages have been reported.

Most of the granite plutons and the mafic intrusions underwent variable degrees of deformations, leading to their gneissic structure and massive structure in the centre part of the plutons (Fig. 3c and e).

3. Pe g a h

3.1. The metamorphic bimodal volcanic rocks

The metamorphic bimodal volcanic rocks are composed of interbedded amphibolite and leptite of variable thickness (Fig. 3a). The leptite is grayish in color and of porphyritic texture. The phenocryst (10%) is subhedral perthite (Fig. 3f). The matrix re-crystallized and mainly comprises of fine-grained feldspar and quartz with minor biotite (Fig. 3f). Due to ductile deformation, some perthite phenocrysts show eyeball forms. The amphibolite is of gneissic structure and granular-lamellar blastic texture. Rock forming minerals include hornblende (25–35%), plagioclase (45–50%), Ti-Fe oxide (10–20%), biotite (2–5%) and minor quartz (less than 2%, Fig. 3 g). According to the rock-forming minerals and the rock association observed in the field, the bimodal volcanic rock series underwent amphibolite facies metamorphism. Two leptite (*meta*-rhyolite) samples (2015D038, 2015D056) were collected for geochronological analysis (longitude-latitude locations of the samples are presented in Supplementary Table 1)

3.2. The trondhjemite-tonalites

In the field, all the granitic plutons could be defined as granodiorite according to their mineral compositions (e.g., low content of quartz). Due to their distinct geochemical features (see following discussions), we divide them into two types. The trondhjemite-tonalites consist of five plutons (Fig. 2) with a total outcropping area of ~ 100 km^2. Most of them are of gneissic structure. They are composed of 45–55% plagioclases (An = 35–45), 5–15% microcline, 15–20% quartz, 10–15% biotite, 5–10% hornblende and accessory minerals, such as zircon, apatite and ilmenite. In thin sections, most rocks show variable alterations, such as the replacement of plagioclase by sericite and replacement of biotite by epidote (Fig. 3 h). Most biotites were likely alteration products of hornblende because these biotites show pseudomorph after hornblende. Some hornblende occurs in the center of the biotite (Fig. 3 h). Fine-grained felsic aggregates and the variable-degreed foliation structure indicate the dynamic metamorphism after their emplacement (Fig. 4). Four geochronological samples were collected from four plutons (2015D029, 2015D035, 2015D037, 2015D070).

3.3. The granodiorite

Only one granodiorite pluton occurs in the western side of Mazar terrane (Fig. 2) with an outcropping area of ~ 8 km^2. It intrudes into the gneissic gabbros and the basement sequence. At its fringe, chrysolite-bearing quartz-feldspar pegmatite dykes can be seen. At one outcrop, the pegmatite dyke sharply cuts the gneissic gabbro (Fig. 3e). The granodiorite mainly comprises of plagioclase (35–45%), microcline (10–20%), quartz (15–25%), K-feldspar (5–10%), biotite (5–10%), hornblende (2–5%) and accessory minerals, such as zircon, apatite and ilmenite. Similar with the scenario of the tonalites, variable degrees of alteration and foliation are commonly seen in thin sections (Fig. 3i). One granodiroite sample (2015D032-1) and one pegmatite sample (2015D032-2) were collected for age determination (Fig. 2).

4. A al ical ced es

Zircon separation was carried out using conventional magnetic and density techniques to concentrate non-magnetic, heavy fractions. Zircon grains were then hand-picked under a binocular microscope. Zircon grains were mounted in epoxy mounts which were then polished to section the crystals in half for analysis. All zircons were documented

Fig. 3. Representative field photographs and petrography of the Archaean metamorphic bimodal volcanic sequence and the Neoproterozoic granitic intrusions in the Mazar terrane. (a) Archaean metamorphic bimodal volcanic sequence (amphibolite – feldspar-quartz letpynite series) at the southwestern section of the Mazar terrane; (b) biotite quartz-feldspar gneiss at the northeastern section of the Mazar terrane; (c) gneissic tonalite; (d) granodiorite intruding into the gneissic gabbros; (e) chrosolite-beating pegmatite intruding into the gneissic gabbros at the margin of the granodiorite pluton; (f) letpynite, showing the perthite phenocryst and re-crystallized matrix mainly composes of fine-grained feldspar and quartz with minor biotite; (g) the amphibolite showing granular-lamellar blastic texture; (h) tonalite, showing the hornblende replaced by epidote and biotite and the sericitization of the plagioclase, (i) granodiorite, dynamic metamorphism induced the fragmentation reaction of the plagioclase and orientation of the biotite. Bi-biotite, Pl-plagioclase, Phl-perthite, Hb-hornblende, Epi-epidote, Q-quartz.

with transmitted and reflected light micrographs as well as cathodoluminescence (CL) images to reveal their morphological appearance and internal structures. Zircon U-Pb ages and Hf isotope compositions were analyzed using the MC-LA-ICP-MS method at the Tianjin Institute of Geology and Mineral Resources (TJGMR), Chinese Geological Survey. A Neptune MC-ICP-MS coupled with a 193 nm excimer laser ablation system were used to determine zircon U–Pb ages. The laser beam diameter was 35 μm and it was operated with a frequency of 10 Hz. Every set of five sample analyses was followed by analysis of the zircon standards 91500 and eight sample analyses followed by the zircon standard GJ-1 (Jackson et al., 2004), and the glass standard NIST610 (see Hou et al., 2009). Each analysis consisted of ca. 5 s of background data acquisition and 45 s of sample data acquisition. $^{207}Pb/^{206}Pb$, $^{206}Pb/^{238}U$, $^{207}Pb/^{235}U$, and $^{208}Pb/^{232}Th$ ratios were corrected for laser and instrumentally induced elemental and isotopic fractionation using zircon GJ-1 as an external standard. Common Pb was corrected using the method proposed by Andersen (2002). The U-Pb concordia plots were processed with ISOPLOT 3.0 and data are presented with 1σ errors and 95% confidence limits (Ludwig, 2003). The zircon U-Pb age data are listed in Supplementary Table 1.

Hf isotope analyses were carried out using a New Wave-193 nm ArF-excimer laser-ablation system linked to a Neptune multiple-collector inductively coupled plasma mass spectrometer (LA-MC-ICP-MS). Instrumental parameters and data acquisition followed that described by Wu et al. (2006) and Geng et al. (2011). The analyses were conducted with a beam diameter of 50 μm, 8 Hz repetition rate with a laser power of 15 J/cm^2. External calibration was made by measuring zircon standard GJ-1 with the unknowns during the analyses to evaluate the reliability of the analytical data. The mean β_{Yb} value was applied for the isobaric interference correction of ^{176}Yb on ^{176}Hf in the same spot. The ratio of $^{176}Yb/^{172}Yb$ (0.5887) was also applied for the Yb correction. A decay constant for ^{176}Lu of 1.865×10^{-11} a^{-1} (Scherer et al., 2001), the present-day chondritic ratios of $^{176}Hf/^{177}Hf = 0.282772$ and $^{176}Lu/^{177}Hf = 0.0332$ (Blichert-Toft and Albarède, 1997) were adopted to calculate $\varepsilon_{Hf}(t)$ values. Single-stage Hf model ages (T_{DM1}) were calculated relative to the depleted mantle present-day value of $^{176}Hf/^{177}Hf = 0.28325$ (Nowell et al., 1998) and $^{176}Lu/^{177}Hf = 0.0384$ (Griffin et al., 2000). The zircon Hf isotopic compositions are listed in Supplementary Table 2.

A total of 28 geochemical samples were collected for major and trace element contents and Sr-Nd isotopic analysis. Major and trace element concentrations were measured at the Institute of Geochemistry (Guiyang), Chinese Academy of Sciences. Major elements were analyzed using a Rigaku ZSX100e XRF following the analytical procedures described by Li et al. (2002). Analytical precision is generally better than 2%. Trace elements were analyzed using a Perkin-Elmer Sciex ELAN 6000 ICP-MS following procedures described by Li et al. (2002). An internal standard solution containing single element Rh was used to monitor signal drift during ion counting. The USGS standards BCR-1, W-2, and G-2, and the Chinese National standards GSR-1 and GSR-3, were used for calibrating element concentrations of measured samples. In-run analytical precision for most elements was generally better than

Fig. 4. Representative cathodoluminescene images of the zircons from the Archaean *meta*-rhyolite and the Neoproterozoic granitic intrusions (see details in the text). The scale bar is 100 μm.

2–5%. The analytical results are presented in Supplementary Table 3.

Sr-Nd isotopes were determined using a Micromass Isoprobe Multi-collector ICPMS (MC-ICPMS) at TJGMR, following the procedure described by Li et al. (2004). Measured $^{87}Sr/^{86}Sr$ and $^{143}Nd/^{144}Nd$ ratios were normalized to $^{86}Sr/^{88}Sr = 0.1194$ and $^{146}Nd/^{144}Nd = 0.7219$, respectively. The reported $^{87}Sr/^{86}Sr$ and $^{143}Nd/^{144}Nd$ ratios were respectively adjusted to the NBS SRM 987 standard $^{87}Sr/^{86}Sr = 0.71025$ and the Shin Etsu JNdi-1 standard $^{143}Nd/^{144}Nd = 0.512115$. Sr-Nd isotope results are listed in Table 4.

5. A al ical es l s

5.1. Zircon U-Pb ages

5.1.1. Age of the Archean volcanic-sedimentary sequence

Zircons from sample 2015D56 range from 80 μm to 150 μm in length and have length to width ratios of 1–2. Most zircon crystals are slight pinkish in color and euhedral or subhedral in form. In CL images, most of them show zoning structure. Some zircons display round form and homogenous inner structure (Fig. 4). Thirty analyses were carried out on 30 grains. Among them, six spots yield significantly older $^{206}Pb/^{238}U$ ages ranging from 2600 Ma to 3270 Ma and they are likely to be xenocrystals. Although four spots on the zircons of homogeneous inner texture yield discordant $^{207}Pb/^{206}Pb$ ages, their $^{206}Pb/^{238}U$ ages are consistent to each other within analytical errors, ranging from 1930 Ma to 1998 Ma with a mean age of 1970 ± 41 Ma (MSWD = 7.3) (Fig. 5a). These four spots have Th contents ranging from 86 ppm to 882 ppm and U from 163 ppm to 1380 ppm with Th/U ratios from 0.5 to 1.1. According to their Th/U ratios, these four zircons were likely igneous zircons. However, their homogeneous inner structure, round form and the large range of Th and U contents share features similar to those of the ca.1.8 Ga metamorphic zircons from the Paleoproterozoic rocks at the northern margin of the Tarim Block (Th/U = 0.7–2.0, Zhang et al., 2012; Long et al., 2010; Ge et al., 2013). Previous studies have demonstrated that the Th/U ratios of metamorphic zircons are controlled by multiple factors, including the crystal growth speed, presence of fluids (Hoskin and Schaltegger, 2001). Zircons which crystallized rapidly in a relatively short time might possess high Th/U ratios up to 0.7 and even up to 3.0 (Vavra et al., 1999; Whitehouse and Kamber, 2002; Santosh et al., 2007). Collectively, we suggest that the 1970 ± 41 Ma age represents a metamorphic event. The other twenty analyses define a good discordant line with an upper intercept age of 2523 ± 23 Ma (MSWD = 0.5, Fig. 5b) and a meaningless lower intercept age of 1484 ± 170 Ma, in spite of variable extents of lead loss.

Twenty-nine analyses were conducted on zircons from sample 2015D038. Among them, three spots yield concordant ages with a mean $^{206}Pb/^{238}U$ age of 2607 ± 31 Ma, likely to be xenocrystals. Four spots on the zircons of homogenous inner texture yield concordant and consistent $^{207}Pb/^{206}Pb$ and $^{206}Pb/^{238}U$ ages with a weighted mean $^{207}Pb/^{206}Pb$ age of 1999 ± 21 Ma (Fig. 5c). The other 22 analyses define a discordia line with an upper intercept age of 2520 ± 31 Ma (MSWD = 0.8, Fig. 5c). On the whole, the results of these two samples are consistent to each other. According to the inner texture and Th/U ratios (0.5–1.0), we conclude that the metamorphic bimodal volcanic sequence formed during the Neoarchean. We noticed that the age data reported by Ji et al. (2011) exhibit variable extents of radiogenic lead loss. We use their original data reported by Ji et al. (2005) and constructed a discordia line with an upper intercept age of 2521 ± 24 Ma (MSWD = 2.1, N = 11). This age is highly consistent with the ages obtained in this study.

5.1.2. Age of the trondhjemite and tonalite

Zircons from sample 2015D029 are of short columnar forms, transparent and colorless or slight yellowish, ranging from 50 μm to 120 μm in length with length/width ratios of 1.5–2. Oscillatory zoning or blurry zoning were observed in CL images (Fig. 4). Thirty-two analyses were conducted on 32 zircon grains. Two spots (2015D029.8, 2015D029.26) yield older but discordant ages, likely to be xenocrystals. The other thirty analyses yield consistent results within analytical error and a weighted mean age of 840.0 ± 3.2 Ma (Fig. 6. N = 30,

MSWD = 0.16).

Zircons from the other 3 trondhjemite-tonalite samples (2015D035, 2015D037, 2015D070) share many common features. They are translucent and colorless. Most grains are prismatic with lengths ranging from 100 to 150 μm and length-width ratios ranging from 2:1 to 3:1 (Fig. 4). In CL images, all zircon grains display oscillatory zoning, indicating their igneous origin. Thirty-two analyses were conducted on each sample (Supplementary table 1). For sample 2015D035, one of the thirty-two analyses (spot 2015D035.7) yields Paleoproterozoic age (1902 ± 22 Ma), likely to be xenocrystal. The other thirty-one analyses show variable U (79–528 ppm) and Th (99–385 ppm) contents with Th/U ratios between 0.6 and 1.0. Their $^{206}Pb/^{238}U$ age and $^{207}Pb/^{235}U$ ages are well concordant within analytical error. They form a tight cluster in the Concordia curve with a weighted mean $^{206}Pb/^{238}U$ age of 839.0 ± 3.1 Ma (Fig. 6b. N = 31, MSWD = 0.32). Among the thirty-two analyses conducted on sample 2015D037, one spot (2015D037.6) yields a slightly younger age for unknown reasons ($^{206}Pb/^{238}U$ age = 787 ± 9 Ma), and other 31 analyses have variable Th and U contents with high Th/U ratios ranging from 0.6 to 1.0, and yield concordant $^{206}Pb/^{238}U$ ages within analytical errors with a weighted mean age of 838.4 ± 3.1 Ma (Fig. 6c. N = 31, MSWD = 0.35). For sample 2015D070, one spot (2015D070.18) of the thirty-two analyses has Neoarchean $^{207}Pb/^{206}Pb$ age (2515 ± 20 Ma), most likely a xenocrystal from the Neoarchean basement of the Mazar terrane (Ji et al., 2011). The other thirty-one analyses yield concordant $^{206}Pb/^{238}U$ ages within analytical errors with a weighted mean age of 835.4 ± 3.1 Ma (Fig. 6d. N = 31, MSWD = 0.53).

5.1.3. Ages of the granodiorite and the pegmatite

Zircons from the granodiorite (2015D032-1) and the pegmatite (2015D032-2) at the margin of the granodiorite pluton resemble each other. They are transparent, colorless, and prismatic with lengths ranging from 100 to 200 μm and aspect ratios ranging from 2:1 to 3:1 (Fig. 4038613.5306Tmpot00r3. N = 2:1 Ma (

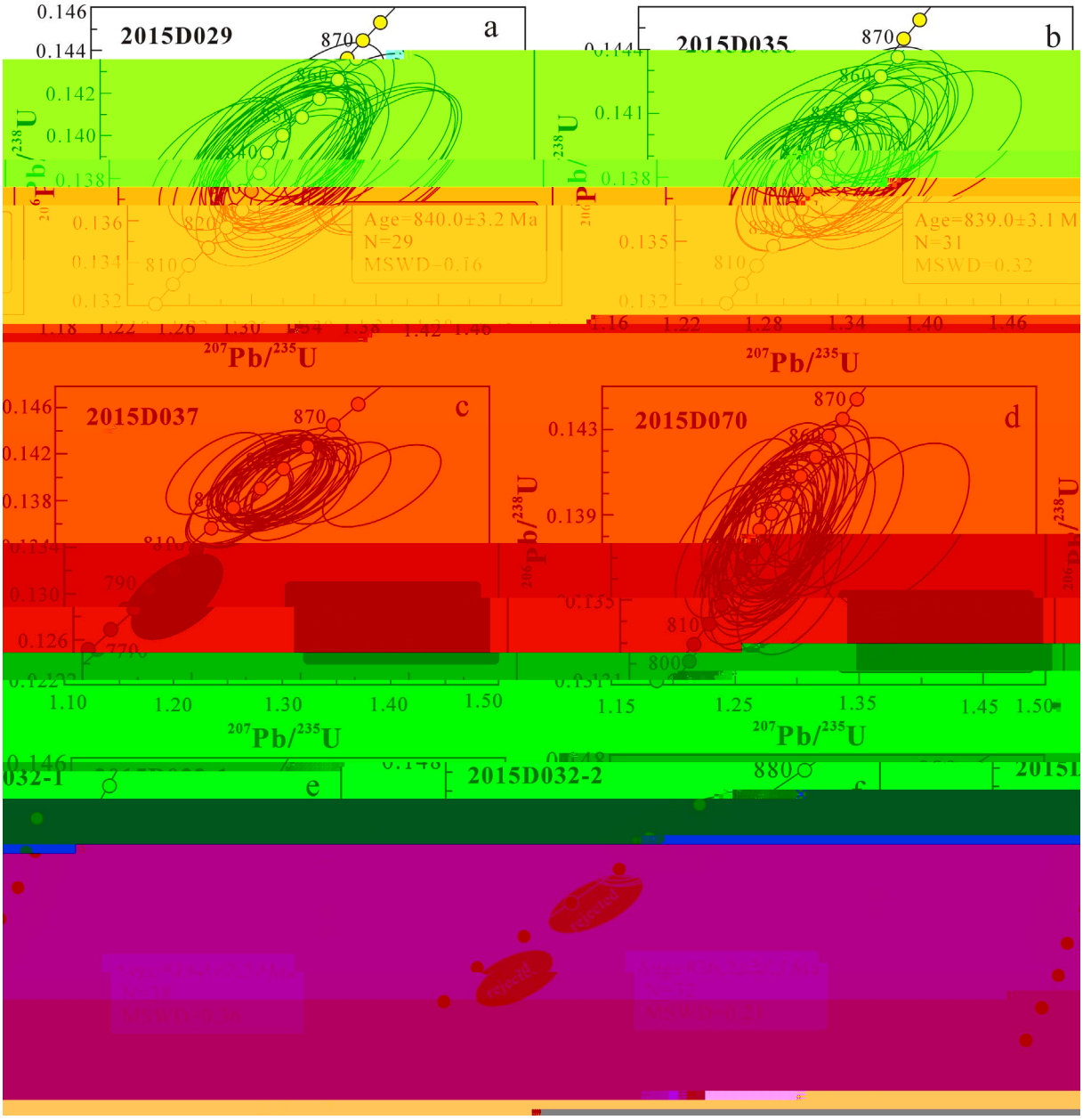

Fig. 6. Concordia of the zircon U-Pb data of the Neoproterozoic granitic intrusions in the Mazar terrane (see details in the text).

contents are generally similar to those of modern adakites and the Archean TTG rocks (Defant and Drummond, 1990; Castllo, 2012).

5.2.2. The granodiorite

Compared with those of the trondhjemite-tonalites, the granodiorite samples have relatively lower and more restricted SiO_2 contents (63–65%). They are metaluminous in nature with A/CNK values ranging from 0.95 to 1.0 (Fig. 7). Their total alkali $Na_2O + K_2O$ ranges from 7.50% to 8.20% and their Na_2O content is similar to K_2O content. By CIPW calculation, in the An–Ab–Or classification diagram, all the samples are plotted into the granodiorite field, which is consistent with thin section observations (Fig. 8). On the Harker diagram, due to restricted chemical compositions, correlations between SiO_2 with other oxides are not significant except that Al_2O_3 and $Fe_2O_3^T$ broadly decrease with increasing SiO_2 content (Fig. 9). Their FeO^T/MgO molar ratios define their medium-Fe nature (Fig. 9) and they have significantly lower Cr (less than 3 ppm) and Ni (5–13 ppm) contents but relatively higher Yb contents (1.8–2.2 ppm), compared with those of the trondhjemite-tonalites. As for trace elements, all samples are enriched in LILE, such as Rb, Ba and Sr, and exhibit negative anomalies in Nb, Ta, P and Ti (Fig. 10d). They have total REE contents ranging from 109 ppm to 157 ppm and are enriched in LREE and depleted in HREE, with consistent $(La/Yb)_N$ ranging from 7 to 11 and insignificant Eu anomalies (Eu∗/Eu = 0.94–1.08) (Fig. 10c). Unlike the trondhjemite-tonalites, the granodiorites have very low Sr/Y ratios (13–28) but higher HREE contents (Supplementary Table 2).

5.3. Zircon Hf isotope compositions

Zircons from the 3 trondhjemite-tonalite samples (2015D029, 2015D035, 2015D037) share similar Hf isotope compositions (Supplementary Table 2, Fig. 11a). Their εHf(t) values are negative, ranging from −14.1 to −9.0, and form a broad Gaussian distribution for these 3 samples (Fig. 11). Furthermore, most analyses yield 1.8–1.9 Ga T_{DM}^{Hf} ages and 3.0–3.2 Ga T_{DM}^{C} ages. On the other hand, the granodiorite sample (2015D032-1) and the pegmatite sample

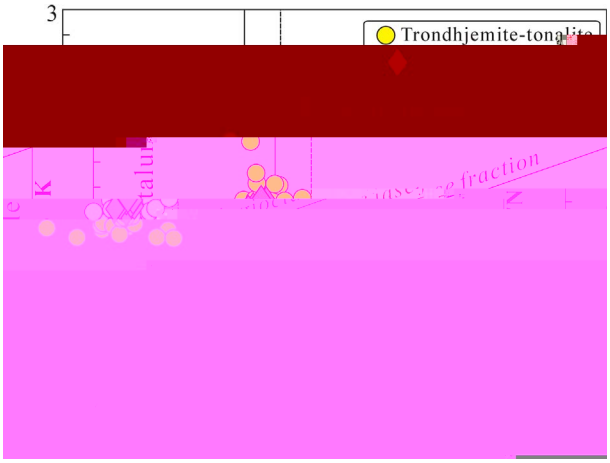

Fig. 7. ACNK vs. ANK diagram showing the metaluminous signature of the trondhjemite-tonalites and the granodiorite.

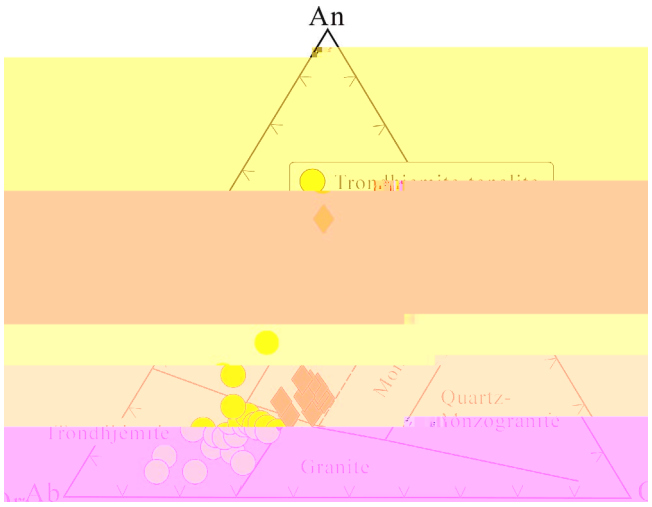

Fig. 8. An-Ab-Or classification diagram of the Neoproterozoic granitic intrusions in Mazar terrane.

(2015D032-2) have slightly higher zircon Hf isotope compositions compared with those of the trondhjemite-tonalites, with εHf(t) values of from −10.9 to −4.5 and from −10 to −2.9, respectively. Nevertheless, these two samples also have similar zircon Hf isotope compositions, e.g., most analyses yield 1.5–1.8 Ga T_{DM}^{Hf} ages and Neoarchean T_{DM}^{C} ages. We combine these two samples and all the analyses form a broad Gaussian distribution with a peak at ~−6 (Fig. 11b). Both the trondhjemite-tonalite and the granodiorite have zircon Hf isotope compositions overlapping that of the Neoproterozoic detrital zircons from the southern margin of the Tarim Block (Fig. 12, Zhang et al., 2016).

5.4. Whole-rock Nd-Sr isotope compositions

Sr-Nd isotope compositions as well as the calculated $(^{87}Sr/^{86}Sr)_i$, εNd(T) and Nd model ages T_{DM} and T_{DM2} for the Neoproterozoic granitic intrusions in Mazar terrane, using the same formulation of Li et al. (2004), are presented in Supplementary Table 4. The trondhjemite-tonalite samples have a narrow range of $^{147}Sm/^{144}Nd$ (0.0930–0.1010) and $^{143}Nd/^{144}Nd$ (0.511834–0.511954) ratios, corresponding to εNd(T) values (T = 840 Ma) ranging from −9.7 to −8.2. The granodiorites have slightly more radiogenic Nd isotope compositions compared with those of the trondhjemite-tonalites (Supplementary Table 4) with εNd(T) values (T = 835 Ma) of ~−5. Due to variable degrees of alterations, both the trondhjemite-tonalites and granodiorites have large range of $(^{87}Sr/^{86}Sr)_i$ values and thus are not used for petrogenetic studies.

6. Discussions

6.1. Petrogenesis of the trondhjemite-tonalites

Chemical compositions of the trondhjemite-tonalites indicate that these rocks are not S-type, M-type, or A-type granites. Their low ferroan and calc-alkalie affinities share most characteristics of the I-type granites (Fig. 9, Frost et al., 2001). On the other hand, their high Sr/Y and $(La/Yb)_N$ ratios, in combination with their very low HREE and HFSE contents, share most features with those of adakitic rocks (Fig. 13) (Defant et al., 2002; Wang et al., 2006), or "High Ba–Sr granites" (Tarney and Jones, 1994; Fowler and Henney, 1996; Fowler et al., 2001; Qian et al., 2002; Chen et al., 2004). Different petrogenetic mechanisms have been proposed for the generation of the adakitic granites or high Ba-Sr granites, including partial melting of a subducting oceanic slab or oceanic plateau (Defant and Drummond, 1990; Kay and Kay, 1993; Stern and Kilian, 1996; Martin et al., 2005); crustal assimilation and fractional crystallization (AFC) processes from parental basaltic magmas (Castillo, 2012); partial melting of a stalled (or dead) slab (or ocean plateau) in the mantle (Pe-Piper and Piper, 1994; Defant et al., 2002; Mungall, 2002; Qu et al., 2004); partial melting of delaminated lower crust (Kay and Kay, 1993; Xu et al., 2002; Wang et al., 2004, 2006) and partial melting of mafic rocks in the lower part of a thickened crust (Atherton and Petford, 1993; Muir et al., 1995; Petford et al., 1996; Xu et al., 2002; Zhang et al., 2007a).

Due to unradiogenic whole-rock Nd and zircon Hf isotope compositions (Supplementary Tables 3 and 4), the trondhjemite-tonalites were unlikely to have been produced by partial melting of subducted oceanic crust. This is consistent with the fact that the trondhjemite-tonalites have remarkably lower $Mg^{\#}$ number and Cr and Ni contents than those of the subducted slab-derived adakites (Fig. 9). AFC processes from parental basaltic magmas can be excluded according to their significant enriched Nd-Hf isotope compositions as well as the AFC curve of mantle-derived magma (Fig. 14, Stern and Kilian, 1996). Partial melting of a stalled (or dead) slab (or ocean plateau) in the mantle, as well as partial melting of delaminated lower crust models could be also ruled out because, the resultant melt rises through a zone of mantle peridotite en route to its emplacement in the upper crust, during which the significant chemical interaction between the mantle peridotite and the crustal melt would enhance the MgO, Cr, Ni contents of the magma and change the whole-rock Nd and zircon Hf isotope compositions. The elemental and isotopic features of the trondhjemite-tonalites, such as their low MgO, Cr and Ni contents and the coupled significant unradiogenic Nd-Hf isotope compositions, are inconsistent with adakitic rocks generated in the above petrogenesis models (Fig. 9).

Numerous studies (Rapp and Watson, 1995; Rapp et al., 1999; Tate and Johnson, 2000; Petford et al., 1996; Petford and Gallagher, 2001; Wang et al., 2006) have demonstrated that mafic crustal rocks may partially melt to generate liquids with high Sr/Y and $(La/Yb)_N$ ratios at sufficient depth (≥30–40 km, *i.e.* ≥ 1–1.2 GPa) where garnet is stable within the residual assemblage (e.g., residues of garnet–amphibolite, amphibole-bearing eclogite and/or eclogite). This model is consistent with the low $Mg^{\#}$, Cr, Ni contents and their coupled unradiogenic Nd-Hf isotope compositions of the studied rocks. In this scenario, the melting temperature can be constrained by the following two factors: (1) it should be higher than 850 °C because dehydration melting of water-unsaturated basaltic rocks could not take place when the temperature is lower than 850 °C (Rapp and Watson, 1995); (2) generally the temperature of the partial melting of the lower crust induced by the underplating of mafic magma is less than 950 °C (Tsuchiya and Kanisawa, 1994). Thus, the trondhjemite-tonalites were most likely generated by partial melting of the mafic lower crust at T = 850–950 °C

and at a pressure with a residue of garnet amphibolite (Fig. 12), corresponding to a depth of 30–40 km.

6.2. *Petrogenesis of the granodiorite*

The I-type geochemical features of the granodiorite preclude that its primitive magma was derived from partial melting of a *meta*-greywacke or clay-rich precursors. Chappell and White (1974) coined the "I-type" term with the implication that the sources were igneous rocks. From experimental and theoretical perspectives, the best candidates for I-type protoliths are not mafic igneous rocks but arc volcanic rocks of intermediate composition (dacites to andesites), and possibly some relatively mafic granodiorites and tonalites that are rich in biotite and hornblende (Clemens et al., 2011). Nevertheless, due to their low SiO_2 contents and sodic nature, intermediate igneous rocks, such as tonalite and granodiorite (or intermediate metamorphic igneous rocks rich in

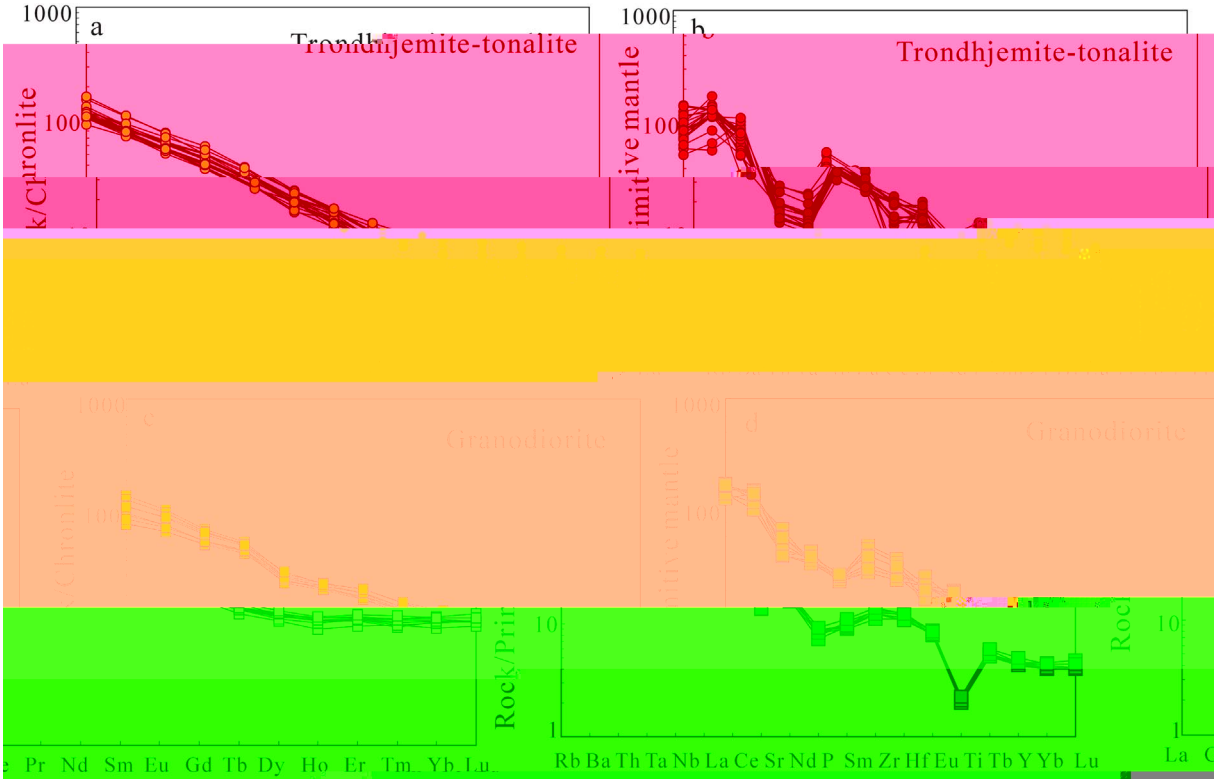

Fig. 10. Chondrite-normalized REE patterns and Primitive mantle -normalized incompatible elements spider diagrams of the Neoproterozoic granitic intrusions (both the Chrondrite and Primitive mantle values are from Sun and McDonough,1989).

We notice that the granodiorites share most major elemental and Nd-Hf isotope features with those of the trondhjemite-tonalites except for their distinct incompatible trace elements compositions (Supplementary Table 3), indicating that their possible similar magma sources but different pressure-temperature condition of partial melting. Having largely ruled out the hybrid model and mantle-derived mafic magma fractionation mechanism, the most suitable magma source for the granodiorite was Precambrian basaltic rocks. However, due to their relatively radiogenetic Nd-Hf isotope compositions and higher $Mg^{\#}$ than those of the trondjemite-tonalites, mantle-derived magma could be involved in the genesis of granodiorite.

Melting experiments of Patiño Douce (1997) demonstrate that shallow dehydration melting of basaltic rocks at > 900 °C generates A-type granites, whereas deep (≥ 8 kbar) dehydration melting generates I-type granites. Nevertheless, compared with the trondhjemite-tonalites, the depth of the partial melting should be shallower than 30 km. Thus, we suggest that the granodiorites were derived from partial melting of a mafic protolith at crustal levels of pressure 8–12 kbar and T > 900 °C.

6.3. Tectonic implications

6.3.1. Tectonic environment of the Neoproterozoic granitic intrusions

It is generally accepted that calc-alkaline I-type granites are genetically related to plate subduction. However, unlike mantle-derived basaltic rocks, the geochemical features of the granites are mainly controlled by the chemical compositions of their crustal sources and pressure–temperature condition of the partial melting. Therefore, they could not be used as a highly robust indicator to decipher the tectonic settings (e.g., Li et al., 2003a). In fact, many studies in recent years have revealed that the I-type granites, even including the adakitic granites, were geodynamically related to extensional environment, such as some Neoproterozoic and Mesozoic granites in South China, the Neoproterozoic adakitic granites in northern margin of Tarim (Zhang et al., 2007a,b; Ye et al., 2008; Li et al., 2003a, 2013).

The elemental signatures, unradiogenic, homogeneous and coupled Nd-Hf isotope compositions of the trondhjemite-tonalites and the granodiorite revealed that they were derived from partial melting of distinct Precambrian basaltic rocks at different depth, excluding the possibility of mantle-derived mafic magma involvement in their genesis. Normal geothermal gradients are seldom sufficient to provide the necessary heat for partial melting of the crust. Crustal doubling, by thrusting or homogeneous thickening, also provides insufficient heat. Extra heat required to induce partial melting of the lower-middle crust is generally ascribed to mantle upwelling and lithosphere extension, possibly through the intrusion and underplating of mafic magmas (Petford and Gallagher, 2001; Clemens, 2003; Li et al., 2003a). This scenario usually takes place during the post-orogenic collapse and continental breakup (Clemens, 2003). It is noted that the granodiorite is slightly younger than the trondhjemite-tonalites. Thus, we tentatively suggest the Neoproterozoic granitic intrusions in Mazar terrane could be formed in an extensional tectonic setting. At the early stage, the mafic magma underplating induced the partial melting of the mafic crust at a depth of ≥ 30 km, and produced the melts with significant adakitic or high Ba-Sr granitic elemental features similar to the voluminous 820–800 Ma adakitic rocks in northern margin of the Tarim Block (Zhang et al., 2007a,b). Due to progressive crustal extension, the partial melting at the middle crust led to the formation of the granodiorite.

6.3.2. The initial breakup of the Rodinia supercontinent

The Rodinian continents, such as Australia, Laurentia, South China, South Korea, India, Seychelles and Tarim, witnessed voluminous and diverse Neoproterozoic (ca. 830–720 Ma) continental intraplate magmatism. This global intraplate magmatism has commonly been attributed to mantle plumes or a superplume that caused the breakup and fragmentation of the supercontinent Rodinia (e.g., Heaman et al., 1992; Park et al., 1995; Li et al., 1999, 2003a, 2008a; Zhao and Cawood, 2012). Generally, initial activity of a mantle plume can produce a large

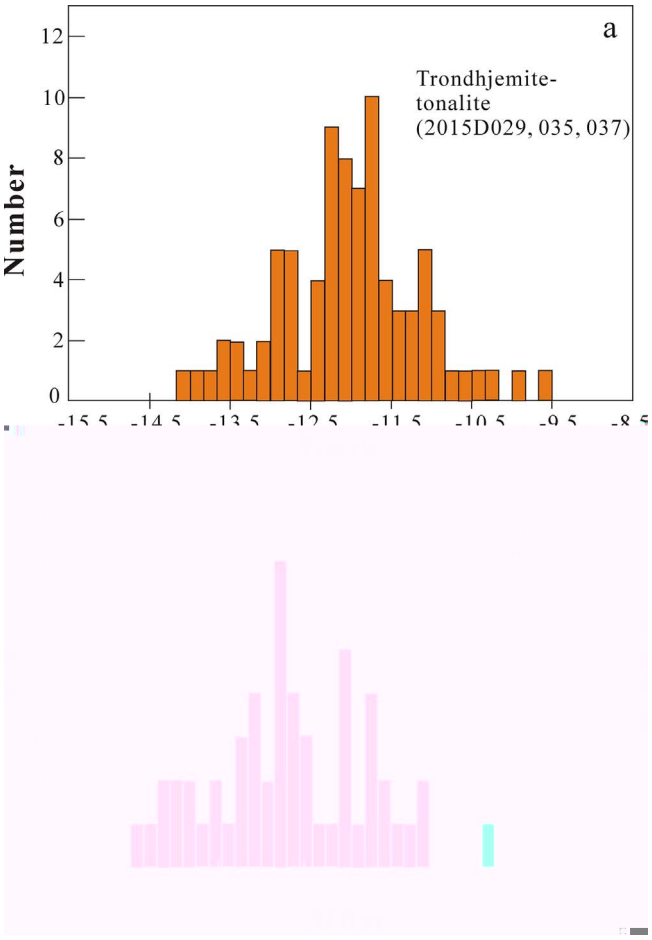

Fig. 11. Histogram of the zircon εHf(t) values of the Neoproterozoic intrusions (see details in the text).

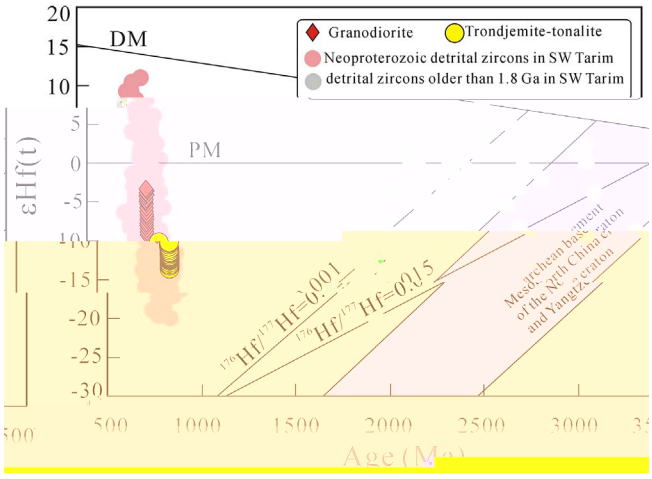

Fig. 12. Crystallization age vs. εHf(t) diagram showing the Hf isotope compositions of the Neoproterozoic trondhjemite-tonalites and granodiorites overlapping with those of the Neoproterozoic detrital zircons in SW Tarim (Zhang et al., 2016).

quantity of basaltic magmas and form continental flood basalts (CFBs) or basaltic plateaus. The "global" onset of the Neoproterozoic mantle superplume is still a matter of debate, although most geologists suggested that the Neoproterozoic mantle plume initiated at ~820 Ma or a little earlier (e.g., Li et al., 1999). The ~850 Ma Shenwu dolerite dykes, the ~ 850 Ma Guandanshan pluton in the western Yangtze Block and the ~ 850 Ma bimodal volcanic sequence in the Cathysia Block were

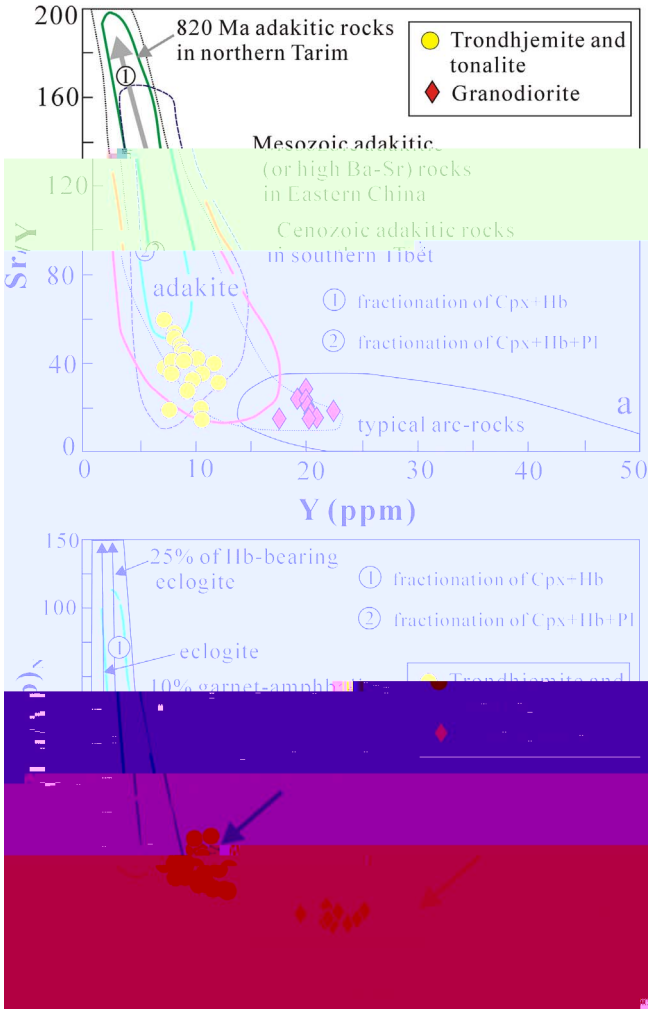

Fig. 13. Sr/Y vs. Y, $(La/Yb)_N$ vs. Yb_N diagrams after Defant and Drummond (1990) (see details in the text).

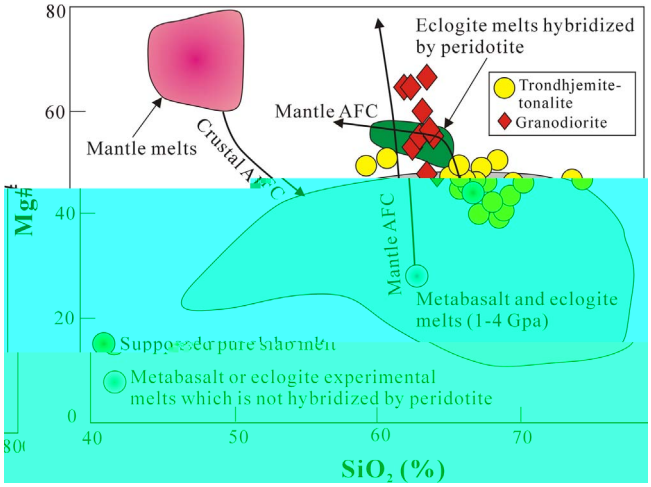

Fig. 14. SiO_2 vs. MgO diagram. The mantle/crustal AFC curves are after Stern and Kilian (1996) (curves 1 and 3) and Rapp et al. (1999) (curve 2). The starting points of curves 1 and 2 represent a pure slab-melt composition and metabasaltic or eclogite experimental melt (Stern and Kilian, 1996) (Rapp et al., 1999), respectively. The field of metabasaltic and eclogite melts (1–4.0 GPa) is after Stern and Kilian (1996). The fields of metabasaltic and eclogite experimental melts that are hybridized with peridotite are after Rapp et al. (1999).

interpreted as the earliest intraplate igneous activity that may be related to the Rodinia breakup (Fig. 15a) (Li et al., 2003b, 2008b, 2008c). In NW China, Song et al. (2010) reported ~850 Ma high-Ti and low-Ti series metamorphic basaltic rocks along the northern margin of the Qaidam Block, and they suggested that those eclogite-facies metamorphic basaltic rocks were part of the earliest dismembered continental flood basalt (CFB) province genetically related to the Rodinia superplume. In the southwestern Tarim Block, 850–830 Ma OIB-like basalts indicate an extensional environment (Fig. 15a, Zhang et al., 2016). 850–840 Ma igneous activities were also observed in Australia, India and South Africa (see Li et al., 2003a and references therein) and these early Neoproterozoic igneous rocks were also interpreted to represent the initial igneous rocks of the Rodinia breakup. Accordingly, we tentatively suggest that the 840–835 Ma granitic intrusions emplaced in the Mazar terrane are genetically related to the Rodinian superplume and that the Mazar terrane could be a continental fragment drifted from the Rodinian continent during its breakup.

6.3.3. Two distinct types of the Precambrian terranes in Tibetan Plateau

According to recent studies, both the Southern Kunlun terrane (SKT) in the eastern section of the Western Kunlun Orogenic Belt and the Taskuergan terrane (TAT) in NE Pamir were early Paleozoic accretionary wedges induced by the Proto-Tethys ocean subduction (Zhang et al., 2007b, 2017a, 2017b). On the other hand, the basement of the Tianshuihai terrane (TST), locally known as Tianshuihai Group, is a low-greenschist facies *meta*-graywacke deposited during the late Neoproterozoic. More importantly, detrital zircon U-Pb dating yielded three significant peaks at ca.890 Ma, ca.805 Ma and ca.750 Ma (Hu et al., 2016; Zhang et al., 2017a). Thus, the Mazar terrane between the north Pamir and the Central Pamir is the only reliable early Precambrian terrane identified in the WKOB.

mafic crust at depth ≥ 30 km whereas the granodiorite formed by partial melting of a mafic crust at shallower level than that of the trondhjemite-tonalites. Their ages and geochemical features suggest that both of them likely formed at an extensional environment.

(4) The 840–835 Ma granitic intrusions distributed in Mazar terrane could be part of the earliest igneous activity related to the initial breakup of the Rodinia supercontinent. The Mazar terrane, as well as the Qilian, Qaidam and Tianshuihai terranes, was likely a continental fragment drifted from Yangtze during its breakup.

Acknowledgements

We sincerely thank Mr. Wen-Hua Ji for his help with the field work and supplying the 1/50000 geological maps. We are grateful to Hong-Ying Zhou for his assistance with LA-ICP-MS zircon dating, and to Zhang Jian for his help with zircon Lu-Hf isotope analyses. This project is funded by the National 305 Project of China (2015BAB05B0X-03) and the Fundamental Research Fund for Central Universities (B16020127). We are grateful to Dr. Wei Wang and an anonymous reviewer for their constructive reviews that greatly improved the quality of this paper.

Appendix A. Supplementary data

Supplementary data associated with this article can be found, in the online version, at http://dx.doi.org/10.1016/j.precamres.2017.11.006.

References

Andersen, T., 2002. Correction of common lead in U-Pb analyses that do not report ^{204}Pb. Chem. Geol. 192, 59–79.
Angiolini, L., Zanchi, A., Zanchetta, S., Nicora, A., Vezzoli, G., 2013. The Cimmerian geopuzzle: new data from South Pamir. Terra Nova 25, 352–360.
Angiolini, L., Zanchi, A., Zanchetta, S., Nicora, A., Vuolo, I., Berra, F., Henderson, C., Malaspina, N., Rettori, R., Vachard, D., Vezzoli, G., 2015. From rift to drift South Pamir (Tajikistan): Permian evolution of a Cimmerian terrane. J. Asian Earth Sci. 102, 148–169.
Atherton, M.P., Petford, N., 1993. Generation of sodium rich magmas from newly underplated basaltic crust. Nature 362, 144–146.
Bian, X.W., Zhu, H.P., Ji, W.H., Cui, J.G., Luo, Q.Z., Ren, J.G., Peng, X.P., 2013. The discovery of Qingbaikouan plutonite in Taxorgan, Xinjiang, and evidence from zircon LA-ICP-MS U-Pb dating of intrusive rock. Northwest Geol. 46, 21–31 (in Chinese with English abstract).
Blichert-Toft, J., Albarède, F., 1997. The Lu-Hf isotope geochemistry of chondrites and the evolution of the mantle-crust system. Earth Planet. Sci. Lett. 148, 243–258.
Boulin, J., 1988. Hercynian and Eocimmerian events in Afghanistan and adjoining regions. Tectonophysics 148, 253–278.
Burtman, V.S., Molnar, P., 1993. . Geological and geophysical evidence for deep subduction of continental crust beneath the pamir. Spec. Pap. Geol. Soc. Am. 281, 76.
Castillo, P.R., 2012. Adakite petrogenesis. Lithos 134–135, 304–316.
Chappell, B.W., White, A.J.R., 1974. Two contrasting granite types. Pac. Geol. 8, 173–174.
Chen, B., Jahn, B.M., Arakawa, Y., Zhai, M.G., 2004. Petrogenesis of the Mesozoic intrusive complexes from the southern Taihang Orogen, North China Craton: elemental and Sr–Nd–Pb isotopic constraints. Contrib. Miner. Petrol. 148, 489–501.
Chen, N.S., Gong, S.L., Sun, M., Li, X.Y., Xia, X.P., Wang, Q.Y., Wu, F.Y., Xu, P., 2009. Precambrian evolution of the Quanji Block, northeastern margin of Tibet: insights from zircon U-Pb and Lu–Hf isotope compositions. J. Asian Earth Sci. 35, 367–376.
Chen, N.S., Zhang, L., Sun, M., Wang, Q.Y., Kusky, T.M., 2012. U-Pb and Hf isotopic compositions of detrital zircons from the paragneisses of the Quanji Massif, NW China: implications for its early tectonic evolutionary history. J. Asian Earth Sci. 54–55, 110–130.
Chen, N.S., Liao, F.X., Wang, L., Santosh, M., Sun, M., Wang, Q.Y., Mustafa, H.A., 2013. Late Paleoproterozoic multiple metamorphic events in the Quanji Massif: links with Tarim and North China cratons and implications for assembly of the Columbia supercontinent. Precambr. Res. 228, 102–116.
Clemens, J.D., 2003. S-type granitic magmas-petrogenetic issue, models and evidence. Lithos 61, 1–18.
Clemens, J.D., Darbyshire, D.P.F., Flinders, J., 2009. Sources of post-orogenic calcalkaline magmas: the Arrochar and Garabal Hill-Glen Fyne complexes, Scotland. Lithos 112, 524–542.
Clemens, J.D., Stevens, G., Farina, F., 2011. The enigmatic sources of I-type granites: the peritectic connexion. Lithos 126, 174–181.
Defant, M.J., Drummond, M.S., 1990. Derivation of some modern arc magmas by melting of young subducted lithosphere. Nature 347, 662–665.
Defant, M.J., Xu, J.F., Kepezhinskas, P., Wang, Q., Zhang, Q., Xiao, L., 2002. Adakites: some variations on the theme. Acta Petrol. Sin. 18, 129–142.
Dewey, J.F., Shackleton, R.M., Chang, C., Sun, Y., 1988. The tectonic evolution of the Tibetan Plateau. Philos. Trans. R Soc. Lond. A 327, 379–413.
Fowler, M.B., Henney, P.J., 1996. Mixed Caledonian appinite magmas: implications for lamprophyre fractionation and high Ba–Sr granite genesis. Contrib. Minerl. Petrol. 126, 199–215.
Fowler, M.B., Henney, P.J., Darbyshire, D.P.F., Greenwood, P.B., 2001. Petrogenesis of high Ba–Sr granites: the Rogart pluton, Sutherland. J. Geolo. Soc., Lon. 158, 521–534.
Frost, B.R., Arculus, R.J., Barnes, C.G., Collins, W.J., Ellis, D.J., Frost, C.D., 2001. A geochemical classification of granitic rock suites. J. Petrol. 42, 2033–2048.
Ge, R.F., Zhu, W.B., Wu, H.L., He, J.W., Zheng, B., 2013. Zircon U–Pb ages and Lu–Hf isotopes of Paleoproterozoic metasedimentary rocks in the Korla Complex, NW China: Implications for metamorphic zircon formation and geological evolution of the Tarim Craton. Precambr. Res. 231, 1–18.
Geng, J.Z., Li, H.K., Zhang, J., Zhang, Y.Q., 2011. Zircon Hf isotope analysis by means of LA-MC-ICP-MS. Geol. Bull. China 30, 1508–1513 (in Chinese with English abstract).
Gibbons, A.D., Zahirovic, S., Müller, R.D., Whittaker, G.M., Yatheesh, V., 2015. A tectonic model reconciling evidence for the collisions between India, Eurasia and intra-oceanic arcs of the central-eastern Tethys. Gondwana Res. 28, 451–492.
Griffin, W.L., Pearson, N.J., Belousova, E., Jackson, S.E., van Achterbergh, E., O'Reilly, S.Y., Shee, S.R., 2000. The Hf isotope composition of cratonic mantle: LAM-MC-ICPMS analysis of zircon megacrysts in kimberlites. Geochim. Cosmochim. Acta. 64, 133–147.
Heaman, L.M., LeCheminant, A.N., Rainbird, R.H., 1992. Nature and timing of Franklin igneous events Canada: implications for a Late Proterozoic mantle plume and the breakup of Laurentia. Earth Planet. Sci. Lett. 109, 117–131.
Hu, J., Wang, H., Huang, C.Y., Tong, L.X., Mu, S.L., Qiu, Z.W., 2016. Geological characteristics and age of the Dahongliutan Fe-ore deposit in the Western Kunlun orogenic belt, Xinjiang, northwestern China. J. Asian Earth Sci. 116, 1–25.
Hoskin, P.W., Schaltegger, U., 2001. The composition of zircon and igneous and metamorphic petrogenesis. Rev. Mineral. Geochem. 53, 25–104.
Hou, K.J., Li, Y.H., Tian, Y.R., 2009. In situ U-Pb zircon dating using laser ablation multi ion counting-ICP-MS. Mineral Deposit. 28, 481–492 (in Chinese with English abstract).
Jackson, S.E., Pearson, N.J., Griffin, W.L., Belousova, E.A., 2004. The application of laser ablation-inductively coupled plasma-mass spectrometry (LA–ICP-MS) to in situ U-Pb zircon geochronology. Chem. Geol. 211, 47–69.
Ji, W.H., Li, R.S., Chen, S.J., He, S.P., Zhao, Z.M., Bian, X.W., Zhu, H.P., Cui, J.G., Ren, J.G., 2011. The discovery of Palaeoproterozoic volcanic rocks in the Bulunkuoler Group from the Tianshuihai Massif in Xinjiang of Northwest China and its geological significance. Sci. China (D-ser.) 54, 61–72.
Jiao, W.F., Wu, Y.B., Yang, S.H., Peng, M., Wang, J., 2009. The oldest basement rock in the Yangtze Craton revealed by zircon U-Pb age and Hf isotope composition. Sci. China D-ser. 52, 1393–1399.
Kay, R.W., Kay, S.M., 1993. Delamination and delamination magmatism. Tectonophysics 219, 177–189.
Kapp, P., DeCelles, P.G., Gehrels, G.E., Heizler, M., Ding, L., 2007. Geological records of the Lhasa-Qiangtang and Indo-Asian collisions in the Nima area of central Tibet. Geol. Soc. Am. Bull. 119, 917–933.
Li, Z.X., Li, X.H., Kinny, P.D., Wang, J., 1999. The breakup of Rodinia: did it start with a mantle plume beneath South China? Earth Planet. Sci. Lett. 173, 171–181.
Li, X.H., Liu, Y., Tu, X.L., Hu, G.Q., Zen, W., 2002. Precise determination of chemical compositions in silicate rocks using ICP-AES and ICP-MS: a comparative study of sample digestion techniques of alkali fusion and acid dissolution. Geochemica 31, 289–294 (in Chinese with English abstract).
Li, X.H., Li, Z.X., Ge, W., Zhou, H., Li, W., Liu, Y., Wingate, M.T.D., 2003a. Neoproterozoic granitoids in South China: crustal melting above a mantle plume at ca. 825 Ma? Precambr. Res. 122, 45–83.
Li, X.H., Li, Z.X., Zhou, H.W., Liu, Y., Liang, X.R., Li, W.X., 2003b. SHRIMP U-Pb zircon age, geochemistry and Nd isotope of the Guandaoshan pluton in SW Sichuan: petrogenesis and tectonic significance. Sci. China Ser. D 46, 73–83.
Li, X.H., Liu, D.Y., Sun, M., Li, W.X., Liang, X.R., Liu, Y., 2004. Precise Sm-Nd and U-Pb isotopic dating of the super-giant Shizhuyuan polymetallic deposit and its host granite; Southeast China. Geol. Mag. 141, 225–231.
Li, Z.X., Bogdanova, S.V., Collins, A.S., Davidson, A., De Waele, B., Ernst, R.E., Fitzsimons, I.C.W., Fuck, R.A., Gladkochub, D.P., Jacobs, J., Karlstrom, K.E., Lu, S., Natapov, L.M., Pease, V., Pisarevsky, S.A., Thrane, K., Vernikovsky, V., 2008a. Assembly, configuration, and breakup history of Rodinia: a synthesis. Precambr. Res. 160, 179–210.
Li, W.X., Li, X.H., Li, Z.X., 2008b. Mid-Neoproterozoic volcanic rocks from the Guangfeng rift succession, South China: U-Pb zircon age, geochemistry, Nd isotope and tectonic significance. Geol. Mag. 145, 475–489.
Li, X.H., Li, W.X., Li, Z.X., Liu, Y., 2008c. 850–790 Ma bimodal volcanic and intrusive rocks in northern Zhejiang South China: a major episode of continental rift magmatism during the breakup of Rodinia. Lithos 102, 341–357.
Li, X.H., Li, Z.X., Li, W.X., Wang, X.C., Gao, Y.Y., 2013. Revisiting the "C-type adakites" of the Lower Yangtze River Belt, central eastern China: In-situ zircon Hf–O isotope and geochemical constraints. Chem. Geol. 345, 1–15.
Li, S.Z., Zhao, S.J., Liu, X., Cao, H., Yu, S., Li, X.Y., Somerville, I., Yu, S.Y., 2017. Closure of the Proto-Tethys Ocean and Early Paleozoic amalgamation of microcontinental blocks in East Asia. Earth-Science Review. In press, at website: https://doi.org /10.1016/j.earscirev.2017.01.011.
Lin, Y.H., Zhang, Z.M., Dong, X., Shen, K., Lu, X., 2013. Precambrian evolution of the Lhasa terrane, Tibet: constraint from the zircon U-Pb geochronology of the gneisses. Precambr. Res. 237, 664–677.
Ling, W.L., Gao, S., Zhang, B.R., Zhou, L., Xu, Q.D., 2001. The recognizing of ca. 1.95 Ga tectono-thermal eventin Kongling nucleus and its significance for the evolution of

Yangtze Block, South China. Chin. Sci. Bull. 46 (4), 326–329.
Long, X.P., Yuan, C., Sun, M., Zhao, G.C., Xiao, W.J., Wang, Y.J., Yang, Y.H., Hu, A.Q., 2010. Archean crustal evolution of the northern Tarim Craton, NW China: Zircon U-Pb and Hf isotopic constraints. Precambr. Res. 180, 272–284.
Ludwig KR. 2003. User's manual for Isoplot 3.00:a geochronological toolkit for Microsoft Excel. Kenneth R. Ludwig.
Lu, S.N., Yu, H.F., Li, H.K., 2006. Research on Precambrian Major Problems in China. Geol. Pub. House 1–206 (in Chinese).
Lu, S.N., Li, H.K., Zhang, C.L., Niu, G.H., 2008. Geological and geochronological evidence for the Precambrian evolution of the Tarim Craton and surrounding continental fragments. Precambr. Res. 160, 94–107.
Martin, H., Smithies, R.H., Rapp, R., Moyen, J.F., Champion, D., 2005. An overview of adakite, tonalite–trondhjemite–granodiorite (TTG) and sanukitoid: relationships and some implications for crustal evolution. Lithos 79, 1–24.
Metcalfe, I., 2011. Palaeozoic-Mesozoic History of SE Asia. In: Hall, R., Cottam, M., Wilson, M. (Eds.), The SE Asian Gateway: History and Tectonics of Australia-Asia Collision. Geological Society of London Special Publications 355, pp. 7–35.
Metcalfe, I., 2013. Gondwana dispersion and Asian accretion: Tectonic and palaeogeographic evolution of eastern Tethys. J. Asian Earth Sci. 66, 1–13.
Meng, Q.X., Zhang, J., Geng, J.Z., Zhang, C.L., Huang, W.C., 2013. Zircon U-Pb age and Hf isotope compositions of Lengjiaxi and Baxi Groups in middle Hunan Province: implications for the Neoproterozoic tectonic evolution in South China. Geol. China 40, 191–216 (in Chinese with English abstract).
Muir, R.J., Weaver, S.D., Bradshaw, J.D., Eby, G.N., Evans, J.A., 1995. Geochemistry of the Cretaceous separation point batholith, New Zealand: granite magmas formed by melting of mafic lithosphere. J. Geol. Soc., Lon. 152, 689–701.
Mungall, J.E., 2002. Roasting the mantle: slab melting and the genesis of major Au and Au-rich Cu deposits. Geology 30, 915–918.
Nowell, G.M., Kempton, P.D., Noble, S.R., Fitton, J.G., Saunders, A.D., Mahoney, J.J., Taylor, R.N., 1998. High precision Hf isotope measurements of MORB and OIB by thermal ionisation mass spectrometry: insights into the depleted mantle. Chem. Geol. 149, 211–233.
Park, J.K., Buchan, K.L., Harlan, S.S., 1995. A proposed giant radiating dyke s.7(by)TJ0-1.2.9(csuchan,)-33uchar31941..7(m7y,)-30-(ma7)-268.7(depleteion)-331(poionisat.4(insightLas)-nt0-(insi-2

Yin, A., Dubey, C.S., Webb, A.A.G., Kelty, T.K., Grove, M., Gehrels, G.E., Burgess, W.P., 2010a. Geological correlation of the Himalayan orogen and Indian craton. Part 1. Structural geology, U-Pb zircon geochronology, and tectonic evolution of theShillong Plateau and its neighbouring regions in NE India. GSA Bull. 122, 336–359.

Yin, A., Dubey, C.S., Kelty, T.K., Webb, A.A.G., Harrison, T.M., Chou, C.Y., Celerier, J., 2010b. Geological correlation of the Himalayan orogen and Indian craton. Part 2. Structural geology, geochronology, and tectonic evolution of the eastern Himalaya. GSA Bull. 122, 360–395.

Yu, S.Y., Zhang, J.X., Li, S.Z., Sun, D.Y., Li, Y.S., Liu, X., Guo, L.L., Suo, Y.H., Peng, Y.B., Zhao, X.L., 2017. Paleoproterozoic granulite-facies metamorphism and anatexis in the Oulongbuluke Block, NW China: Respond to assembly of the Columbia super-continent. Precambr. Res. 291, 42–62.

Zanchi, A., Poli, S., Fumagalli, P., Gaetani, M., 2000. Mantle exhumation along the Tirich Mir Fault Zone, NW Pakistan: Pre-mid-Cretaceous accretion of the Karakoram terrane to the Asian margin, in Tectonics of the Nanga Parbat Syntaxis and the Western Himalaya, edited by M. A. Khan et al., Geol. Soc. Spec. Publ., 170, 219–236.

Zanchi, A., Gaetani, M., 2011. The geology of the Karakoram range, Pakistan: the new 1:100,000 geological map of Central-Western Karakoram. Italy J. Geosci. 130, 161–262.

Zhao, G.C., Cawood, P.A., Wilde, S.A., Sun, M., 2002. Review of global 2.1–1. 8 Ga orogens: implications for a pre-Rodinia supercontinent. Earth-Sci. Rev. 59, 125–162.

Zhao, G.C., Cawood, P.A., Wilde, S.A., Sun, M., Zhang, J., He, Y.H., Yin, C.Q., 2012. Amalgamation of the North China Craton: key issues and discussion. Precambr. Res. 222–223, 55–76.

Zhao, G.C., Cawood, P.A., 2012. Precambrian geology of China. Precambr. Res. 222–223, 13–54.

Zhang, S.B., Zheng, Y.F., Wu, Y.B., Zhao, Z.F., Gao, S., Wu, F.Y., 2006. Zircon U-Pb age and Hf isotope evidence for 3.8 Ga crustal remnant and episodic reworking of Archean crust in South China. Earth Planet. Sci. Lett. 252, 56–71.

Zhang, C.L., Li, X.H., Li, Z.X., Lu, S.N., Ye, H.M., Li, H.M., 2007a. Neoproterozoic ultra-mafic–mafic-carbonatite complex and granitoids in Quruqtagh of northeastern Tarim Block, western China: geochronology, geochemistry and tectonic implications. Precambr. Res. 152, 149–169.

Zhang, C.L., Lu, S.N., Yu, H.F., Ye, H.M., 2007b. Tectonic evolution of Western Orogenic belt: evidences from zircon SHRIMP and LA-ICP-MS U-Pb ages. Sci. China (D) 50, 1–12.

Zhang, C.L., Li, H.K., Zou, H.B., 2013b. Tectonic framework and evolution of the Tarim Block in NW China. Gondwana Res. 23, 1306–1315.

Zhang, C.L., Zou, H.B., Santosh, M., Ye, X.T., Li, H.K., 2014a. Is the Precambrian base-ment of the Tarim Craton in NW China composed of discrete terranes? Precambr. Res. 254, 226–244.

Zhang, C.L., Santosh, M., Zhu, Q.B., Chen, X.Y., Huang, W.C., 2015. The Gondwana connection of South China: evidence from monazite and zircon geochronology in the Cathaysia Block. Gondwana Res. 28, 1137–1151.

Zhang, C.L., Ye, X.T., Zou, H.B., Chen, X.Y., 2016. Neoproterozoic sedimentary basin evolution in southwestern Tarim, NW China: new evidence from field observations, detrital zircon U-Pb ages and Hf isotope compositions. Precambr. Res. 280, 31–45.

Zhang, C.L., Zou, H.B., Ye, X.T., Chen, X.Y., 2017a. Tectonic evolution of the eastern section of Western Kunlun Orogenic Belt at the northern margin of the Tibetan Plateau: new evidence from field observations and geochronology. Gondwana Res under review.

Zhang, C.L., Zou, H.B., Ye, X.T., Chen, X.Y., 2017b. Tectonic evolution of the NE section of the Pamir Plateau: new evidences from field observation and zircon U-Pb geo-chronology. Tectonophysics under review.

Zhang, J.X., Yu, S.Y., Gong, J.H., Li, H.K., Hou, K.J., 2013a. The latest Neoarchean –Paleoproterozoic evolution of the Dunhuang block, eastern Tarim craton, north-western China: Evidence from zircon U-Pb dating and Hf isotopicanalyses. Precambr. Res. 226, 21–42.

Zhang, L., Wang, Q.Y., Chen, N.S., Sun, M., Santosh, M., Ba, J., 2014b. Geochemistry and detrital zircon U-Pb and Hf isotopes of the paragneiss suite from the Quanji massif, SE Tarim Craton: implications for Paleoproterozoic tectonics in NWChina. J. Asian Earth Sci. 95, 33–50.

Zhang, Z.M., Zhao, G.C., Santosh, M., Wang, J.L., Dong, X., Liou, J.G., 2010. Two stages of granulite facies metamorphism in the eastern Himalayan syntaxis, south Tibet: pet-rology, zircon geochronology and implications for the subduction of Neo-Tethys and the Indian continent beneath Asia. J. Metamorph. Geol. 28, 719–733.

Zhang, Z.M., Dong, X., Santosh, M., Liu, F., Wang, W., Yiu, F., He, Z.Y., Shen, K., 2012. Petrology and geochronology of the Namche Barwa Complex in the eastern Himalayan syntaxis, Tibet: Constraints on the origin and evolution of the north-eastern margin of the Indian Craton. Gondwana Res. 21, 123–137.

Zhu, D.C., Zhao, Z.D., Niu, Y.L., Dilek, Y., Wang, Q., Ji, W.H., Dong, G.C., Sui, Q.L., Liu, Y.S., Yuan, H.L., Mo, X.X., 2012. ian Craton92012.